Nonlinear response of a ballistic graphene transistor with an ac-driven gate: High harmonic generation and terahertz detection

Y. Korniyenko,[1] O. Shevtsov,[2] and T. Löfwander[1]
[1]*Department of Microtechnology and Nanoscience - MC2, Chalmers University of Technology, SE-412 96 Göteborg, Sweden*
[2]*Department of Physics & Astronomy, Northwestern University, Evanston, Illinois 60208, USA*
(Received 14 July 2016; published 30 September 2016)

We present results for time-dependent electron transport in a ballistic graphene field-effect transistor with an ac-driven gate. Nonlinear response to the ac drive is derived utilizing Floquet theory for scattering states in combination with Landauer-Büttiker theory for transport. We identify two regimes that can be useful for applications: (i) low and (ii) high doping of graphene under source and drain contacts, relative to the doping level in the graphene channel, which in an experiment can be varied by a back gate. In both regimes, inelastic scattering induced by the ac drive can excite quasibound states in the channel that leads to resonance promotion of higher-order sidebands. Already for weak to intermediate ac drive strength, this leads to a substantial change in the direct current between source and drain. For strong ac drive with frequency Ω, we compute the higher harmonics of frequencies $n\Omega$ (n integer) in the source-drain conductance. In regime (ii), we show that particular harmonics (for instance, $n = 6$) can be selectively enhanced by tuning the doping level in the channel or by tuning the drive strength. We propose that the device operated in the weak-drive regime can be used to detect THz radiation, while in the strong-drive regime, it can be used as a frequency multiplier.

DOI: 10.1103/PhysRevB.94.125445

I. INTRODUCTION

Graphene for analog high-frequency electronics has been the focus of intense research over the last few years, and is one of the focus areas in the recently published graphene road map [1]. Two dimensionality of the material, high carrier mobility, gate-tunable charge density, and a unique band structure with massless Dirac electrons are a few of the properties that make graphene a promising material in this context [2–6]. Examples of devices already produced, with competitive figures of merit, are field-effect transistors [7], frequency doublers [8], frequency mixers [9], and detectors [10–13].

The electronic mobility has been constantly improving and ballistic electron transport is today studied intensively. Ballistic transport allows for development of massless Dirac electron optics, which is the graphene analog of usual optics. Electron optics effects that have been observed include Fabry-Pérot interferences and snake states [14], Veselago lensing [15], and so-called whispering gallery modes in circular p-n junctions [16].

For ballistic devices, evidence of hydrodynamic behavior has been recently presented: viscous electron backflow [17] and breakdown of the Wideman-Franz law [18,19]. This indicates that due to the long elastic mean free path, and slow electron-phonon relaxation below room temperature, electron-electron interactions can be the most dominant scattering channel within a certain temperature window. However, at sufficiently low temperatures (below 100 K), electron-electron interactions also become weak and, ultimately, at lower temperature, transport is truly ballistic over long (μm) length scales.

Improved mobility (possibly reaching ballistic transport) is a necessary condition for the development of high-frequency devices. There has therefore been a broad interest in the theory of time-dependent transport in graphene in the ballistic transport regime, including quantum pumping [20–23], nonlinear electromagnetic response [24–33], and photon-assisted tunneling [34–40]. In the nonclassical regime, when the energy scale $\hbar\Omega$, set by the drive frequency Ω ($\hbar$ is Planck's constant divided by 2π), and the Fermi energy E_F, measured relative to the charge-neutrality point, are of comparable magnitude, a variety of interesting quantum mechanical interference and resonance effects become important. In a recent paper [41], we have studied in detail a Fano resonance [38–40,42] induced by a quasibound state on the top-gate barrier. We showed how it could be utilized to develop a frequency doubler for weak or moderate ac drive strength. In this paper, we extend this study to include a more realistic doping profile across the device as well as strong ac drive. Within a fully quantum mechanical treatment based on Floquet theory and Landauer-Büttiker scattering theory [42–45], we show how Fano resonances as well as resonant tunneling can be utilized for detection of high-frequency radiation in the THz range or to generate high harmonics of the ac signal.

The outline of the paper is as follows. In Sec. II, we give details of the model and the methods of calculations. This section also includes a characterization of the dc regime as a prologue to the discussions of time-dependent transport in the following chapter, as well as a detailed discussion of the relation between the different parameters of the model and various possible transport regimes. In Sec. III, we present results for the weak ac drive regime, with focus on high-frequency radiation detection. In Sec. IV, we present the result for the strong ac drive regime, with focus on high harmonic generation. Section V summarizes the paper. A few technical results are collected in the Appendix.

II. MODEL

Our goal is to establish a relation between intrinsic electronic transport properties of a ballistic graphene transistor, depicted in Fig. 1(a), and experimentally controllable physical parameters. Extrinsic (parasitic) effects due to eventual

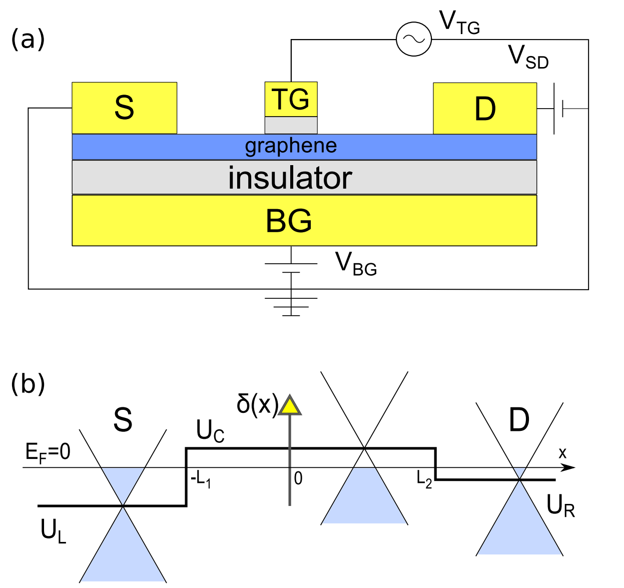

FIG. 1. (a) Schematics of a graphene field-effect transistor, where a back gate (BG) controls doping of the channel, and a small source-drain (S-D) bias is applied to generate the current, which is controlled by the top-gate (TG) dc and ac signals. (b) Potential landscape, including doping of the leads by the source and drain metallic electrodes.

surrounding circuit elements must be dealt with when doing experiments, but can be neglected in an attempt to describe the intrinsic properties. We make a minimal model based on a number of assumptions that we outline in the following.

First, we assume that the contacts and gates are ideal, such that they can be described by the potential landscape sketched in Fig. 1(b). We take into account that the source and drain metallic contacts dope graphene underneath due to work function mismatches. The doping levels, set by U_L and U_R, in the graphene source and drain areas are thereby pinned [46]. On the other hand, in the transistor channel region, $x \in [-L_1, L_2]$, the doping level can be tuned by the back-gate potential. We define the channel Dirac point energy by setting $E_D = U_C$ [assuming absence of electron-hole (e-h) puddles], where U_C can be tuned by the back gate. Since we measure energies with respect to the Fermi level $E_F = 0$ (aligned with the metallic contact Fermi energies), the Dirac point in the channel region is aligned with the Fermi energy for $U_C = 0$ (the channel is then charge neutral). In summary, the doping profile sketched in Fig. 1(b) is given by

$$U(x) = U_L\theta(-L_1 - x) + U_R\theta(x - L_2) + U_C[\theta(x + L_1) - \theta(x - L_2)]. \quad (1)$$

We assume that the top gate is wide on the scale of the C-C bond length a_{cc}, but short on the scale that the envelope of the Dirac electron wave function varies, which is given by $\lambda_D = \hbar v_F/(E - U_C)$, where v_F is the Fermi velocity. For energies E near the Dirac point in the channel, we have $\lambda_D \gg a_{cc}$. Based on the same arguments, we assume that the doping level is changing slowly near the contacts on the a_{cc} scale, but fast on the scale of λ_D. These assumptions mean that we can neglect intervalley scattering in the problem and consider only one valley. For transport quantities, a factor two for valley degeneracy is included in addition to the factor two for spin degeneracy. The above assumptions also allow us to use step functions for the doping profile, as in Eq. (1), and a δ barrier model for the top-gate potential. The effective low-energy Hamiltonian then has the form

$$\mathcal{H} = -i\sigma_x\nabla_x + \sigma_y k_y + [Z_0 + Z_1\cos(\Omega t)]\delta(x) + U(x), \quad (2)$$

where we have set the Fermi velocity in graphene equal to unity, $v_F = 1$, and $\hbar = 1$. The Pauli matrices in pseudospin space (A-B sublattices) are denoted by σ_x and σ_y. We assume the device to be very wide and translationally invariant along y. Thus any edge effects are negligibly small and transverse momentum k_y is (approximately) conserved. Above, Z_0 and Z_1 are, respectively, the static and dynamic parts of the drive applied at the top gate. The δ-function description of the top-gate barrier is obtained as a limiting case of a very high $V \to \infty$ and narrow $D \to 0$ square barrier, with the product (barrier strength) $VD = Z$ constant. Note that this theory for the Dirac quasiparticle envelope wave function holds as long as $a_{cc} \ll D \ll \lambda_D$.

Wave-function solutions have to satisfy the time-dependent Dirac equation

$$\mathcal{H}\psi(x,k_y,t) = i\partial_t\psi(x,k_y,t). \quad (3)$$

The harmonic potential, with frequency Ω, in the Hamiltonian $\mathcal{H}$ in Eq. (2) allows us to use a Fourier decomposition and construct a Floquet ansatz,

$$\psi(x,k_y,t) = e^{-iEt}\sum_{n=-\infty}^{\infty}\psi_n(x,k_y,E)e^{-in\Omega t}, \quad (4)$$

where amplitudes at sideband energies $E_n = E + n\Omega$ (n integer) are the result of the charge carrier picking up (or giving up) energy quanta $n\Omega$ from the oscillating barrier. The quasienergy E is set by the energy of the particle incident from the source electrode in the scattering problem. When plugged into Eq. (3), it yields a set of coupled differential equations for sideband amplitudes $\psi_n(x,k_y,E)$. The solutions can be derived in a straightforward manner by wave-function matching and collected into a Floquet scattering matrix describing scattering of a quasiparticle incoming from the left or right reservoir at energy E and transverse momentum k_y. We have collected all the key steps of the derivation in the Appendix. The reflection amplitudes $r_n(k_y,E)$ are given in Eq. (B10) and the transmission amplitudes $t_n(k_y,E)$ are given in Eq. (B11).

Following the Landauer-Büttiker scattering approach, the Floquet scattering matrix can be used to compute the time-dependent conductance $G(t)$ between source and drain. The conductance is computed in linear response to the source-drain voltage V_{SD}, but in nonlinear response to the oscillating top-gate potential, described by its drive strength Z_1 and frequency Ω. The conductance is also a function of the static potential landscape, described by $U(x)$, as well as the static top-gate potential quantified by its barrier strength Z_0. We derived the general formula for $G(t)$ in Ref. [41]. Here we choose to present results for the linear conductance in the right lead at $x = L_2^+$, i.e., at the interface with the channel region. The expression for the conductance (per unit length in the transverse direction) at zero temperature is then [47]

$$G(E_F,t) = \sum_{n=-\infty}^{\infty} G_n(E_F) e^{-in\Omega t}, \tag{5}$$

$$G_n(E_F) = G^*_{-n}(E_F), \tag{6}$$

$$G_n(E_F) = \frac{4e^2}{h} \int_{-\infty}^{\infty} \frac{dk_y}{2\pi} \sum_{m=-\infty}^{\infty} \times \frac{\eta^*(k_y,E_m - U_R) + \eta(k_y,E_{n+m} - U_R)}{2\sqrt{v(k_y,E_m - U_R)v(k_y,E_{n+m} - U_R)}} \times e^{i[\kappa(k_y,E_m-U_R)-\kappa(k_y,E_{n+m}-U_R)]\times L_2} \times t^\dagger_m(k_y,E) t_{n+m}(k_y,E)|_{E=E_F}, \tag{7}$$

where $\eta(k_y,E)$, $v(k_y,E)$, and $\kappa(k_y,E)$ are defined in Eq. (A5). The factor with velocities appears here because we utilize a scattering basis where elementary waves in the leads carry unit probability flux. This guarantees that the scattering matrix coupling incoming and outgoing waves in the leads is unitary. The phase of the conductance components G_n for $n \neq 0$ is unimportant for our discussion and we will present results for $|G_n|$ below. Note that in the static case (i.e., $Z_1 = 0$), the factor with velocities as well as the phase factor both reduce to unity and the usual Landauer-Büttiker formula for dc conductance simply in terms of transmission is obtained.

In the rest of the paper, we shall report results for a symmetric setup with $L_1 = L_2 = L/2$ and symmetric doping profile $U_L = U_R = U$. The transmission probabilities are computed for zero back-gate voltage, i.e., $U_C = 0$, as a function of energy E and transverse momentum $k_y = |E - U| \sin\varphi$ parametrized by an impact angle φ. This means that $E = 0$ corresponds to transmission at the Dirac point in the channel region. This is a conventional way to present transmission through a potential landscape. On the other hand, the zero-temperature linear conductance, computed via Eq. (7), shall be presented as a function of the channel doping U_C (the position of the Dirac point energy E_D). In an experiment, the channel doping level can be tuned by the back-gate voltage V_{BG}. Since the Fermi energy is pinned to the metallic source and drain contact Fermi energies, the radius of the Dirac cone in the graphene leads is constant, set by the doping level U, while the radius in the channel is given by U_C and varies with back-gate voltage. This choice should correspond to the experimental situation.

A. Dc characteristics

We start by analyzing the static case ($Z_1 = 0$) in order to set the stage for the signatures of the time-dependent drive that we will study in the following sections. It is useful to first look at the case with no applied top-gate potential $Z_0 = 0$, thereby highlighting the effect of the inhomogeneous doping profile. In fact, $U(x)$ describes a square barrier across the channel of width $L = L_1 + L_2$. We plot the transmission probability $T_0(E,\varphi)$ in Fig. 2(a). The transmission amplitude is governed by pseudospin matching between regions with different doping. For small angles φ, the mismatch is negligibly small, thus transmission approaches unity (Klein tunneling).

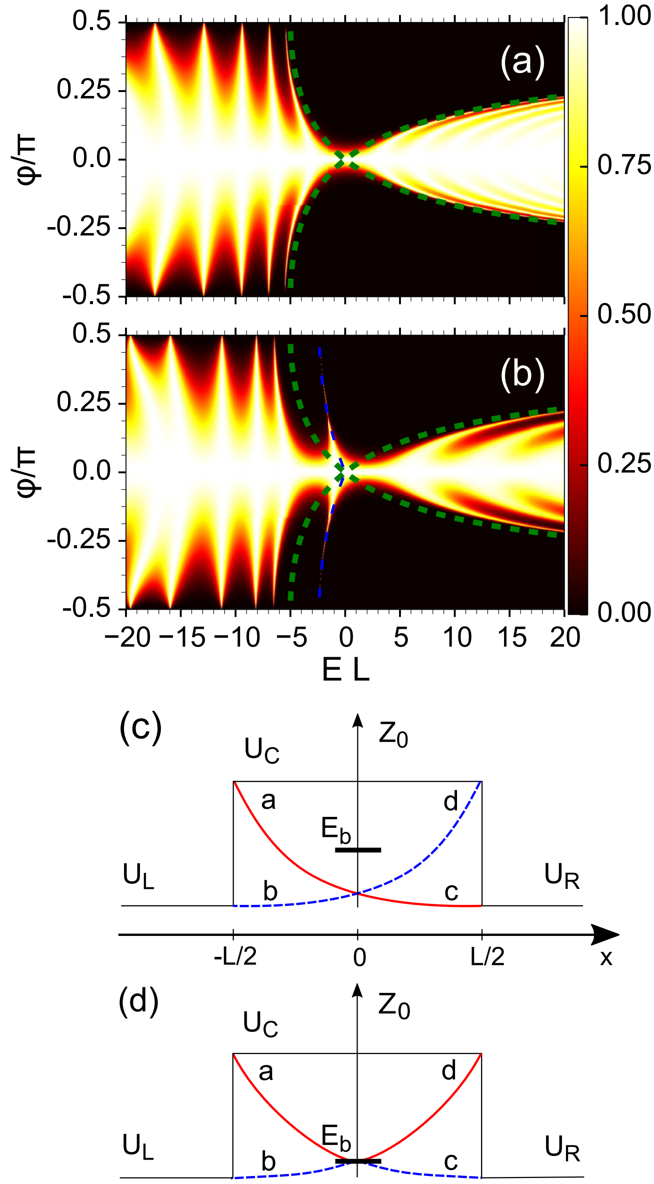

FIG. 2. (a) Dc transmission probability as a function of energy and incidence angle. Electrodes are doped at $U = -10/L$, while the gate potentials are zero such that $Z_0 = 0$ and $U_C = 0$. Green dashed lines indicate boundaries to evanescent regions $|\varphi| > \varphi_c$. (b) Transmission probability in the presence of a top-gate dc potential, $Z_0 = 0.4\pi$. Blue long-dashed lines indicate resonant tunneling. (c), (d) The connection between evanescent waves at the δ barrier for off- and on-resonance tunneling, respectively.

The peaks in transmission for large angles φ and negative energies $E < -5/L$ in Fig. 2(a) are analogous to Fabry-Pérot fringes, i.e., the result of wave interference between two partially reflecting mirrors (boundaries at the source and drain in this case). A typical fringe oscillation period is of the order of $2\pi\hbar v_f/L$ (reinstating the units). In addition to the two effects described above, there is a large region where transmission is largely suppressed. It occurs when the waves in the channel region are evanescent. Their longitudinal momentum component $\kappa(k_y,E) = \pm\sqrt{E^2 - k_y^2}$ turns imaginary, giving us a condition on the critical angle of incidence φ_c,

$$\varphi_c = \arcsin\left|\frac{E}{E-U}\right|. \quad (8)$$

For any $|\varphi| > \varphi_c$, the waves injected from the electrodes are evanescent in the channel ($x \in [-L_1, L_2]$). Note that Eq. (8) holds for $|E| < |E-U|$. Otherwise there are no evanescent waves involved in transport and we may put $\varphi_c = \pi/2$. The boundary between propagating wave transport and evanescent wave transport is indicated by a green dashed line in Fig. 2(a). The evanescent wave factor $\exp(-\sqrt{k_y^2 - E^2}L)$ lowers the transmission probability in general. However, for energies close to the Dirac point and small k_y (or small L), this factor is still quite large and evanescent waves can reach between the two contacts, thus giving rise to large transmission probability. Transport at $E = 0$ is achieved exclusively through evanescent waves. This is the so-called pseudodiffusive transport regime [48].

When we introduce the static top-gate δ-barrier potential, $Z_0 \neq 0$, additional features appear in the transmission. First, the Fabry-Pérot oscillations are shifted due to an additional phase shift at the δ barrier; see Fig. 2(b). More importantly, the δ barrier can host one bound state at energy

$$E_b = U_C - \mathrm{sgn}(Z_0)|k_y|\cos Z_0, \quad (9)$$

which we studied for $U(x) = 0$ in Ref. [41]. In that case, the bound state does not affect dc transport properties, but can be excited by ac drive. Here, for finite electrode doping $U \neq 0$, the bound state can be excited already in dc. In fact, in this case, it is not a true bound state, rather a quasibound state with evanescent waves in the channel region connected to propagating waves in the leads. In Fig. 2(b), we see that the resonance in $T_0(E,\varphi)$ originates at $E = 0$ and then disperses with the angle of incidence φ. The resonance can be understood in analogy with widely studied resonant double-barrier tunneling [49,50] in Schrödinger quantum mechanics. In the analogy, the two barriers correspond in our case to the two channel regions between the contacts and the top-gate δ barrier, and the resonant level between the barriers corresponds in our case to the quasibound state in the δ barrier. A complementary point of view of the resonance can be found in the equations; see Appendix A 3. Off resonance, exponentially decaying waves with amplitudes a and c are connected, as sketched in Fig. 2(c). This results in an exponentially small transmission amplitude. On the other hand, when the quasibound state is hit, the exponentially decaying wave with amplitude a on one side of the δ barrier is coupled only to an exponentially rising solution with amplitude d on the other side, as sketched in Fig. 2(d). The exponential functions thereby cancel in the expression for the transmission which leads to resonance behavior [cf. Eq. (A28)].

For the calculation of the conductance in Eq. (7), we need to integrate the transmission probability over angles. In an attempt to describe the typical experimental situation, we assume that the Fermi energy in the device and the doping levels in the leads are pinned by the Fermi energy in the metal contacts, while the back gate can be used to tune the doping level in the channel. The zero-temperature conductance as a function of U_C is then computed by integrating the transmission function $T(E,\varphi;U_L,U_R,U_C)$ over angles at fixed energy $E = 0$ (Fermi energy) and fixed U_L and U_R. We plot the corresponding view of the angle-dependent transmission function in Figs. 3(a) and 3(b). Note that in Fig. 2, we plotted $T(E,\varphi;U_L,U_R,U_C)$ as a function of E and φ for fixed $U_C = 0$ and fixed U_L and U_R. The transmission function as viewed in Figs. 3(a) and 3(b) corresponds to leads that are electron doped (here, $U = -10/L$). Thus, both incoming waves and scattered waves in the leads are electronlike (n type) at the Fermi energy $E_F = 0$. For $U_C < 0$, we have electronlike waves at $E_F = 0$ in the channel, while for $U_C > 0$, we have holelike waves in the channel (p type). Therefore, the Fabry-Pérot interference patterns for positive U_C (n-p-n junction) and negative U_C (n-n'-n junction) are different.

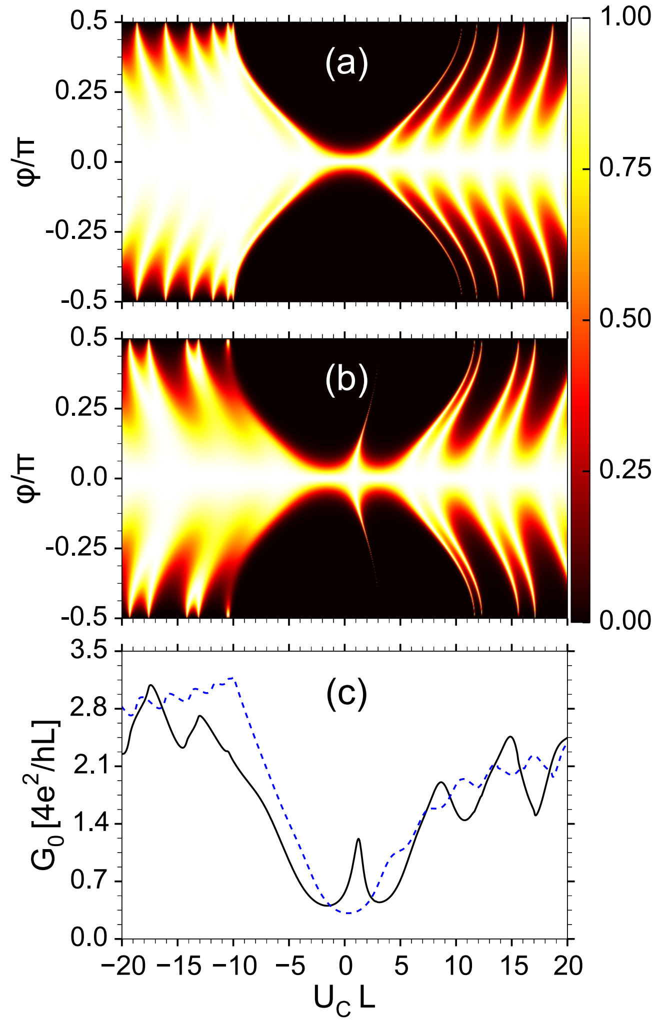

FIG. 3. (a) Transmission probability in the absence of top-gate barrier ($Z_0 = 0$) for electrodes with pinned doping levels set by $U = -10/L$, and varying channel doping level U_C, which defines the position of the Dirac point relative to the Fermi energy $E_F = 0$. (b) The transmission probability including a top-gate barrier of strength $Z_0 = 0.4\pi$. (c) Corresponding angle-integrated dc linear conductances for $Z_0 = 0$ (blue dashed line) and for $Z_0 = 0.4\pi$ (solid black line).

In Fig. 3(c), we present the dc conductance as a function of channel doping level U_C. For $|U_C| < |U|$, we have mainly

TABLE I. Energy scales within our model and relevant parameters that determine them.

U	contact doping levels $U_R = U_L = U$
U_C	channel doping level
$\hbar v_F/L$	channel length $L = L_1 + L_2$
$\hbar v_F/\Delta L$	channel asymmetry $\Delta L = \lvert L_1 - L_2\rvert$
$\hbar\Omega$	drive frequency Ω

evanescent mode transport, while for larger values of $|U_C|$, we find oscillations due to the Fabry-Pérot interferences. The resonance peak near $U_C = 0$ (solid black line for finite Z_0) is due to the δ-barrier-induced quasibound state.

B. Parameter regimes

Starting from the dc characterization above, we can identify several parameter regimes. They can be described by different relations between the relevant energy scales in the problem, listed in Table I. In the dc characterization above, we used $\hbar v_F/L$ as the energy scale. Note that with $v_F = 1 = \hbar$, energies are measured in units of L^{-1}. In addition to the relations between the energy scales in Table I, we have to take into account the oscillating δ-barrier strength Z_1.

The observed regimes in dc are (cf. Fig. 3) as follows:

(I) $|U_C| \geqslant |U|$: propagating wave transport.

(a) $|U| \sim \hbar v_F/L$: clearly visible Fabry-Pérot interferences as a function of U_C with period approximately given by $2\pi\hbar v_F/L$;

(b) $|U| \gg \hbar v_F/L$: very fast oscillations that in reality would be washed out by inhomogeneity or temperature smearing;

(c) $|U| \ll \hbar v_F/L$: the oscillations are too slow (on the scale of $U_C \sim U$) to be observed.

(II) $|U_C| \ll |U|$: evanescent wave transport (pseudodiffusive regime).

(a) $U \ll \hbar v_F/\Delta L$: resonant tunneling is possible when the channel is not too asymmetric.

The dc drive strength Z_0 sets the position of the quasibound state in the resonant tunneling regime and shifts the Fabry-Pérot oscillations, but does not define a regime by itself. We note that both the evanescent wave regime [51] and the Fabry-Pérot regime [14] have been observed experimentally.

Under the ac drive, we will in the next sections investigate the following regimes:

(III) $Z_1 < 1$: Weak to intermediate drive.

(a) $\hbar\Omega \gtrsim U$, low contact doping; with (Ia) above: Fano and Breit-Wigner resonances;

(b) $\hbar\Omega < U$, high contact doping; with (IIa) above: inelastic resonant tunneling.

(IV) $Z_1 > 1$: Strong drive.

(a) $\hbar\Omega \gtrsim U$, low contact doping; with (Ia) above: multiple Fano and Breit-Wigner resonances;

(b) $\hbar\Omega < U$, high contact doping; with (IIa) above: inelastic resonant tunneling and high harmonic generation.

We can estimate from experiments the typical parameter values. Contact doping (parameter U) has been reported [52,53] in the range of -100 to 100 meV (corresponding to doping levels of up to 10^{12} cm^{-2}, either n or p type). Typical device channel lengths are from 10 nm to 1 μm, making the corresponding energy scale $\hbar v_f/L$ in the range of 1–100 meV. The corresponding ballistic flight time from source to drain is $\tau = L/v_F$ and is about 1 ps. We note in passing that within Landauer-Büttiker scattering theory, all relaxation times must then be longer than this, which is the case at low temperature and low energies in a ballistic device (mobility $\mu \geqslant 10^5$ cm^2/V s). The driving frequency, $\hbar\Omega$, is between 0.4–40 meV for the THz frequency range 0.1–10 THz. The drive strength Z_1, for $Z_1 \sim 1$, corresponds to a voltage of the order of a meV on the top gate for typical gate lengths (see the estimate in our previous paper [41]). Finally, in the following, we assume that temperature is the smallest energy scale (we put $T = 0$). With these numbers, all parameter regimes listed above are within experimental reach.

III. WEAK TO INTERMEDIATE DRIVE, $Z_1 < 1$

A. Low contact doping: Fano and Breit-Wigner resonances

In Ref. [41], we studied the case when $\hbar v_F/L$ is the smallest energy scale, i.e., the channel is long. We were then allowed to assume that evanescent waves cannot reach between the contacts and the δ barrier. In practice, we set $U(x) = 0$, and let $L \to \infty$. In these limits, we studied Fano and Breit-Wigner resonances induced by the δ-barrier quasibound state and argued that they can be used to enhance the second harmonic. In the more general formalism introduced here, we can ask what a small amount of contact doping $U \neq 0$ leads to. We present in Figs. 4(a) and 4(b) the transmission probabilities $T_0(E,\varphi)$ and $T_2(E,\varphi)$ for a small amount of contact doping and large distance to contacts, $|U| = \hbar v_F/L = 0.01\Omega$. Compared with the results in Ref. [41], we find a small wedge of evanescent wave transport in an energy window around $E = 0$ (outside the green dashed lines). The transmission of propagating waves displays fast Fabry-Pérot interferences. The Fano resonance in T_0 and the Breit-Wigner resonance in T_2 [processes sketched in Fig. 4(c)] are, however, not affected. For increasing contact doping (larger $|U|$), the Fabry-Pérot oscillations get stronger and will eventually interfere with the Fano and Breit-Wigner resonances, but not destroy them. This holds as long as $\hbar v_F/L \ll \Omega$. For shorter contacts, the wedge of evanescent wave transport around $E = 0$ widens. When $\hbar v_F/L$ and Ω are of comparable magnitude, the most important feature in the transmission is instead resonant inelastic tunneling.

B. High contact doping: Inelastic resonant tunnelling

Let us next consider the resonant tunneling regime. We assume a symmetric device with $L_1 = L_2$, with highly doped leads, and weakly doped channel, $|U_C| \ll |U|$, such that we have evanescent wave transport through the device. The resonance due to the quasibound state in the δ barrier studied for dc transport above will also create resonant inelastic tunneling under ac drive. The resonance condition for weak drive $Z_1 \ll 1$ is $n\Omega = E_b$. This leads to promotion of higher-order sidebands as well as higher harmonics in the conductance that we will study below.

In Fig. 5, we present the transmission probabilities T_n for $n = 0, \pm 1$, and 2. For T_0 in Fig. 5(a), two new transmission

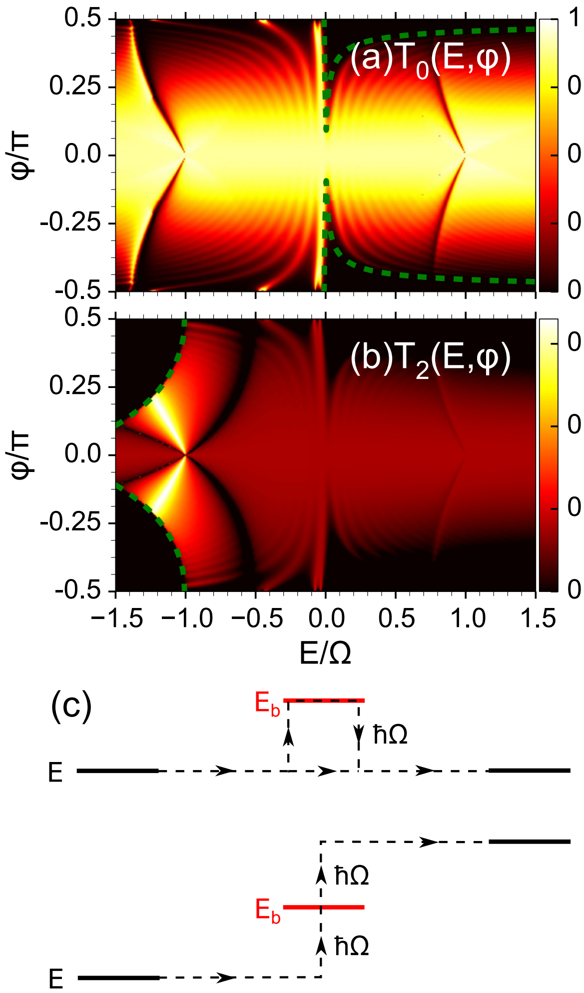

FIG. 4. (a) Direct transmission probability $T_0(E,\varphi)$ and (b) transmission probability to the second sideband $T_2(E,\varphi)$ for parameters corresponding to Fig. 2 in Ref. [41] ($Z_0 = 0.4\pi$, $Z_1 = 0.45$), but including a small doping of contact leads $U = -0.01\Omega$ relative to the channel ($U_C = 0$). The device is long, such that $\hbar v_F/L = 0.01\Omega$. (c) Sketches of the Fano resonance process and the inelastic Breit-Wigner resonance process identified in Ref. [41] to be responsible for the dip-peak structure in T_0 and the peak in T_2, respectively.

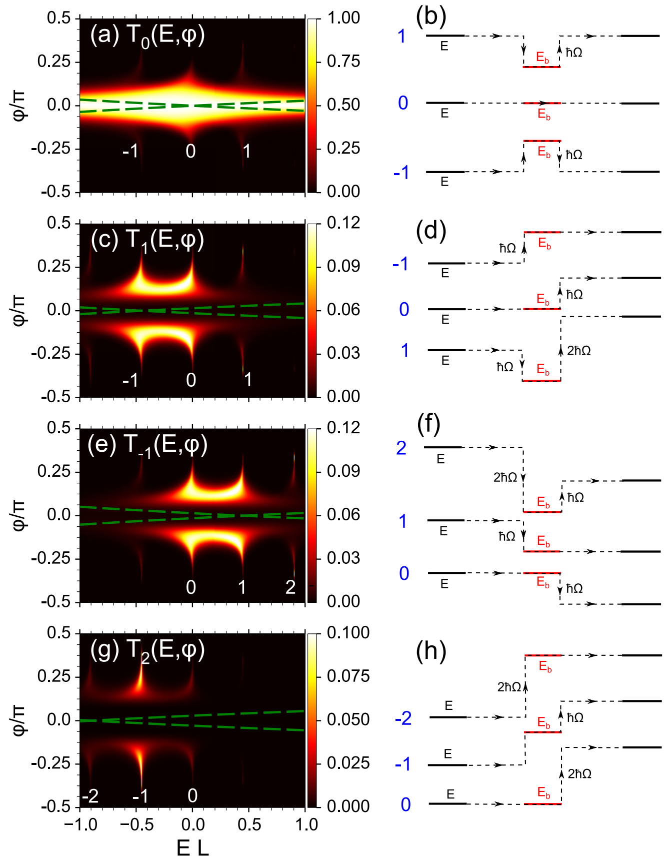

FIG. 5. Resonant transmission via evanescent waves for elastic transmission ($n = 0$) and inelastic transmission to sideband energies ($n = \pm 1$ and $n = 2$). The parameters are $U = -10/L$, $\Omega = 0.45/L$, $Z_0 = 0.5\pi$, and $Z_1 = 0.1$.

peaks emerge, separated by $\pm\Omega$ from the main (0th) peak present already in dc. The side peaks emerge because of the possibility of absorbing/emitting energy quanta, as shown in Fig. 5(b). In the evanescent region, multiple sideband energies can now satisfy the bound state requirement, thus resulting in a number of resonant peaks separated roughly by Ω (for $Z_0 \approx \pi/2$). Generally, these peaks are weaker than the one in the static case, since the bound-state contribution is now spread across several channels. Analogous processes are involved during inelastic scattering between sidebands, as illustrated in Figs. 5(c) and 5(d) for T_1, Figs. 5(e) and 5(f) for T_{-1}, and Figs. 5(g) and 5(h) for T_2.

In Fig. 6, we present the dc conductance G_0 as a function of channel doping U_C for increasing ac drive strength Z_1. The inelastic resonant tunneling processes discussed above for transmission probabilities result in side peaks in the conductance spaced by multiples of Ω from the main resonance peak present in dc. Already for rather weak drive $Z_0 \sim 0.1$, several peaks are visible and the main elastic peak is reduced. This can be traced to the energy dependence in the matrix on the left-hand side in Eq. (B11), which is given by a combination of functions in Eq. (A5), all inversely proportional to energy. The bound-state energy $|E_b - U_C|$ is small, which results in division of small numbers and enhanced effective coupling of sidebands close to the resonance energy. Thus, the range of validity of a perturbative approach in small Z_1 is limited.

In the literature, when systems other than graphene have been studied, the conductance is often presented as a function of ac drive frequency [45]. That is natural since there is often no knob corresponding to the very convenient back gate which can be used to tune the graphene channel doping level (i.e., the parameter U_C varied above). For comparison, we present in Fig. 7 the dc conductance for varying frequency, keeping the doping level $U_C = 1/L$, i.e., a hole-doped channel. In this case, we find conductance peaks at frequencies such that a sideband coincides with the quasibound state, i.e., $n\Omega = E_b$. Higher-order processes are weaker for weak drive strength Z_1, thus the resonance peaks have smaller amplitudes and widths.

Considering Figs. 6 and 7 together, it is clear that the device can be used as a tunable detector. The frequency Ω of the signal that needs to be detected tells us which channel doping we should choose (tunable by the back gate), such that the first

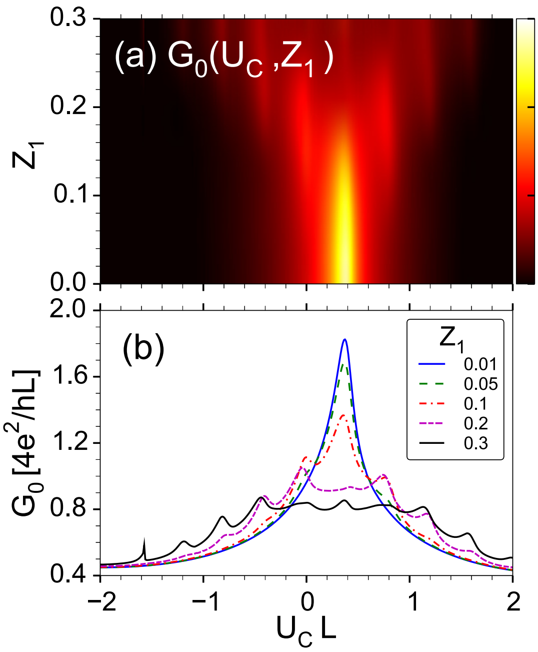

FIG. 6. (a) Dc conductance under ac drive of varying strength Z_1 in a range of channel dopings U_C corresponding to evanescent wave transport. The resonance peak for dc is reduced under ac drive and side peaks spaced by multiples of Ω appear due to resonant inelastic tunneling. (b) Horizontal cuts in the color map in (a) at particular values of Z_1. The parameters are $Z_0 = 0.48\pi$, $U = -10/L$, and $\Omega = 0.4/L$.

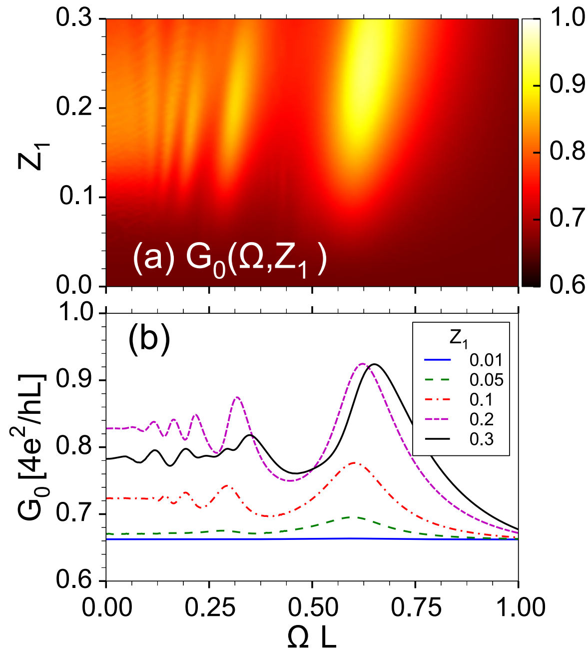

FIG. 7. (a) Dc conductance under varying ac drive frequency Ω for the same parameters as in Fig. 6, but with fixed channel doping $U_C = 1/L$. Inelastic tunneling resonance peaks appear when a sideband coincides with the quasibound state.

sideband is resonant. Then the dc conductance is monitored to detect the signal.

IV. STRONG DRIVE, $Z_1 > 1$

To understand the system behavior at strong drive, it is useful to look at the transmission probability behavior as a function of driving strength Z_1. Since the δ-barrier boundary condition matrix $\check{M}$ is directly related to Bessel functions of the first kind in sideband space [see Eq. (C10)], we can expect transmission amplitudes to also follow the corresponding Bessel functions. To illustrate the point, we introduce normalized angle-integrated transmissions,

$$\tau_n(U_C,Z_1) = \frac{\int d\varphi\, T_n(\varphi,U_C,Z_1)}{\int d\varphi\, T_0(\varphi,U_C,Z_1=0)}. \qquad (10)$$

Indeed, the general behavior of τ_n for constant U_C follows that of $J_n^2(Z_1)$; see Fig. 8. Next, let us discuss how the resonances described above for weak drive evolve for strong drive, bearing in mind that the distribution of sideband amplitudes is in simplified terms given by Bessel functions.

A. Low contact doping

First, we would like to discuss the evolution of Fano and Breit-Wigner resonances described above for low doping U of contacts. We observe multiple Fano resonances (cf. Fig. 9) that are due to the bound-state condition satisfied by sideband waves in the contacts. It is useful to note that since we fixed the energy $E_F = 0$ and have U_C as our parameter, the evanescent wave region boundaries for sideband n become horizontal lines, given by $|\varphi| = \phi_c^n$, where

$$\phi_c^n = \arcsin\left|\frac{n\Omega - U}{U}\right|. \qquad (11)$$

Note that this equation holds for $|n\Omega - U| < |U|$. Otherwise, waves are propagating in the contacts for all φ and we can set $\phi_c^n = \pi/2$. To avoid confusion, we emphasize that ϕ_c^n in Eq. (11) defines critical angles for evanescent sideband waves in the contacts (which do not contribute to transport), while φ_c in Eq. (8) defines a critical angle for evanescent waves in the channel (which do contribute to transport). For parameters used in Fig. 9, only $n = 1$ and 2 sidebands have evanescent regions. The corresponding Fano and Breit-Wigner resonances

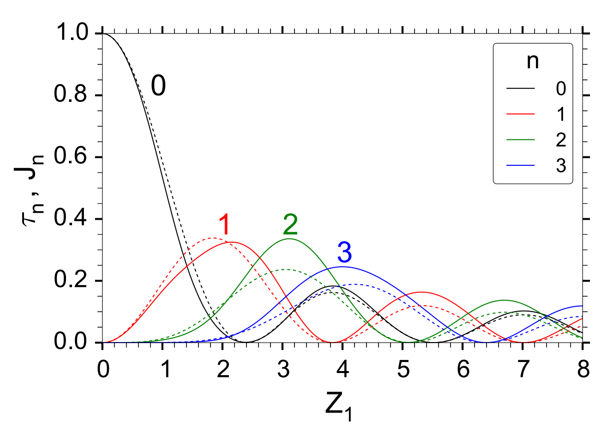

FIG. 8. Bessel functions envelopes (dashed lines) and normalized angle-integrated sideband transmissions T_n (solid lines) for $U_C = -9/L$. The parameters are $U = -10/L$, $Z_0 = 0.4\pi$, and $\Omega = 1/L$.

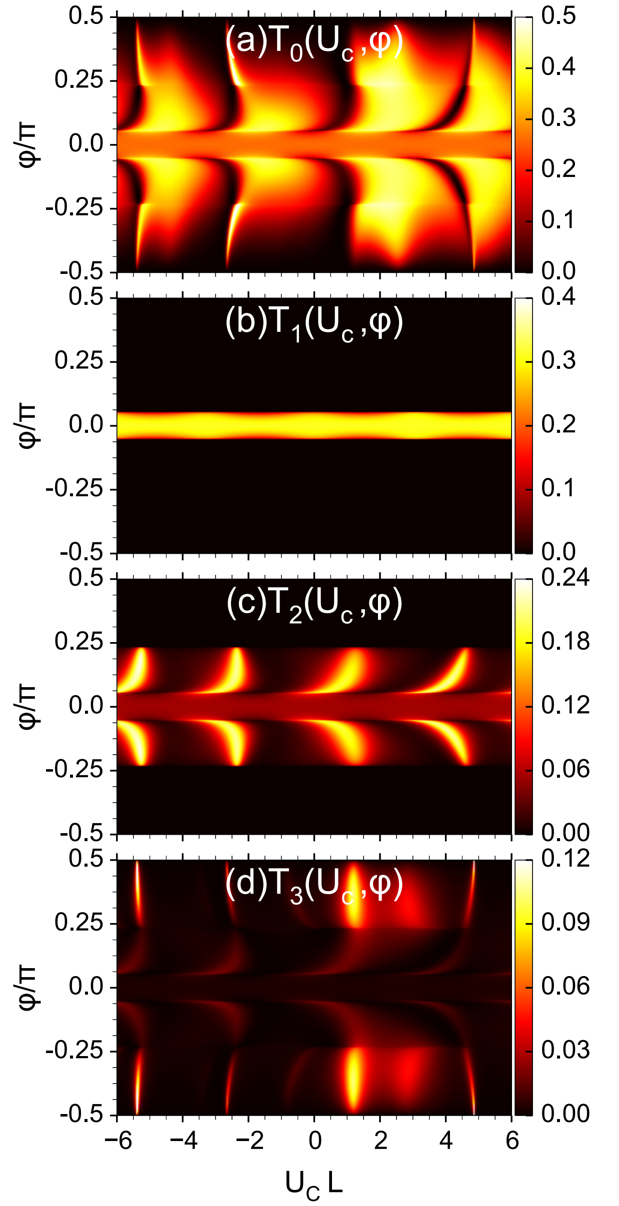

FIG. 9. Transmission functions $T_n(U_C,\varphi)$ for strong drive $Z_1 = 1.5$ and low contact doping $U = 1.2/L$. The drive frequency is $\Omega = 1/L$ and the static barrier strength is $Z_0 = 0.4\pi$.

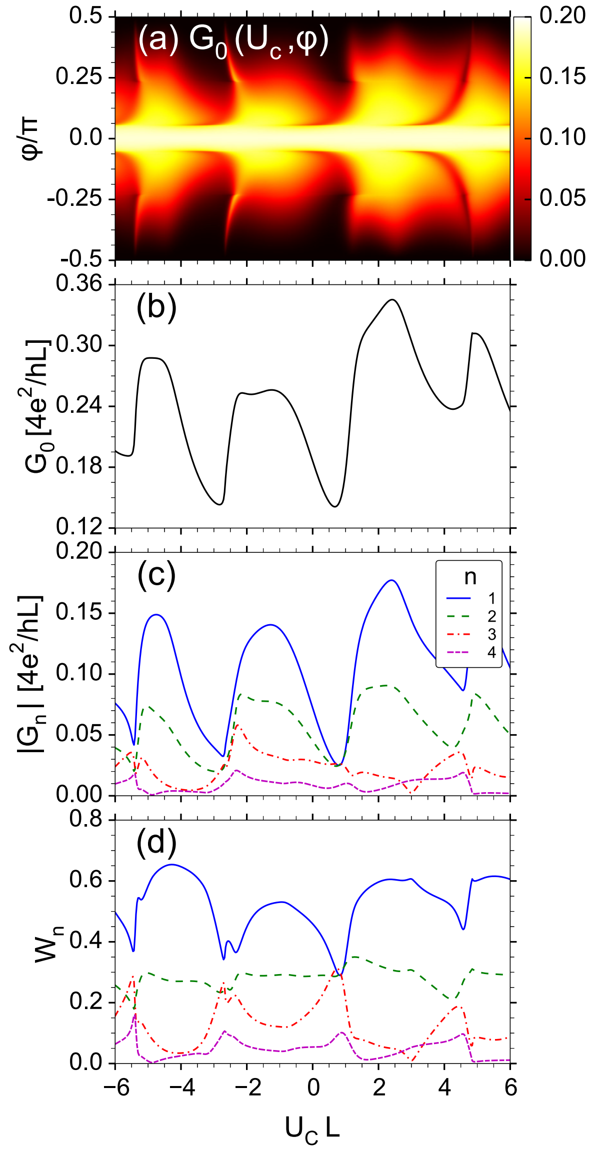

FIG. 10. (a) Angle-resolved and (b) angle-integrated dc conductance for the same parameters as in Fig. 9. (c) First four ac harmonics and (d) the relative weight of ac harmonics as defined in Eq. (12).

now originate at the critical angle boundary and disperse with the angle of incidence. As has been shown in our previous work [41], Fano resonances broaden as Z_1^2 and their positions change as the driving strength is increased. We note also that due to the strong coupling between sidebands for $Z_1 > 1$, the evanescent region boundary is clearly visible across all transmission channels. Unlike in the weak driving case, the zeroth transmission channel stops being dominant and thus higher sidebands are increasingly important in the conductance calculation.

Given the strong separation between evanescent and propagating wave regions as a function of angles in transmissions, it leads to a similar pronounced behavior in angle-resolved conductances, as shown in Fig. 10(a) for the dc component. After integration over angles, we observe clear oscillations in the U_C dependence of the dc conductance [see Fig. 10(b)], which are due to the multiple Fano resonances discussed above. The second and third harmonics are of equal size as the first harmonic for U_c corresponding to the resonances; see Fig. 10(c).

It is useful to define a quantitative estimate of the relative power of ac harmonics as

$$W_n = \frac{|G_n|}{\sum_{n=1}^{\infty} |G_n|}, \quad n \geqslant 1. \tag{12}$$

For simplicity, we exclude negative n harmonics in this estimate, since we know that $G_{-n} = G_n^*$. In Ref. [41], we discussed weak drive and second harmonic generation. In Fig. 10(d), we show for strong drive $Z_1 = 1.5$ that both the second and third harmonic can be resonantly enhanced and become of the same order as the first harmonic for the case $|U_C| > |U|$. Higher harmonics $n > 3$ are, however,

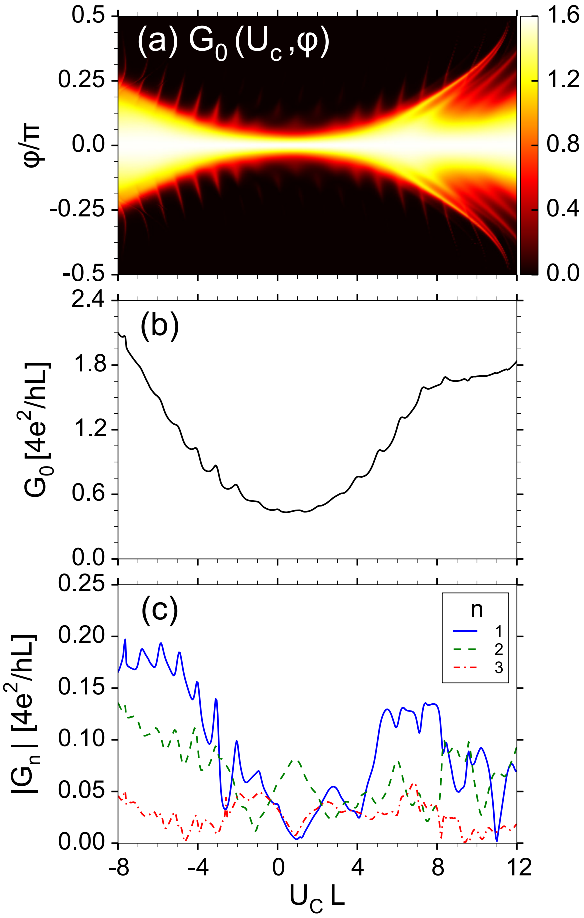

FIG. 11. (a) Angle-resolved, and (b) angle-integrated dc conductance for high contact doping $U = -10/L$ and strong drive $Z_1 = 1.5$. (c) First few ac harmonics for the same parameters. The drive frequency is $\Omega = 1/L$ and the static barrier strength is $Z_0 = 0.4\pi$.

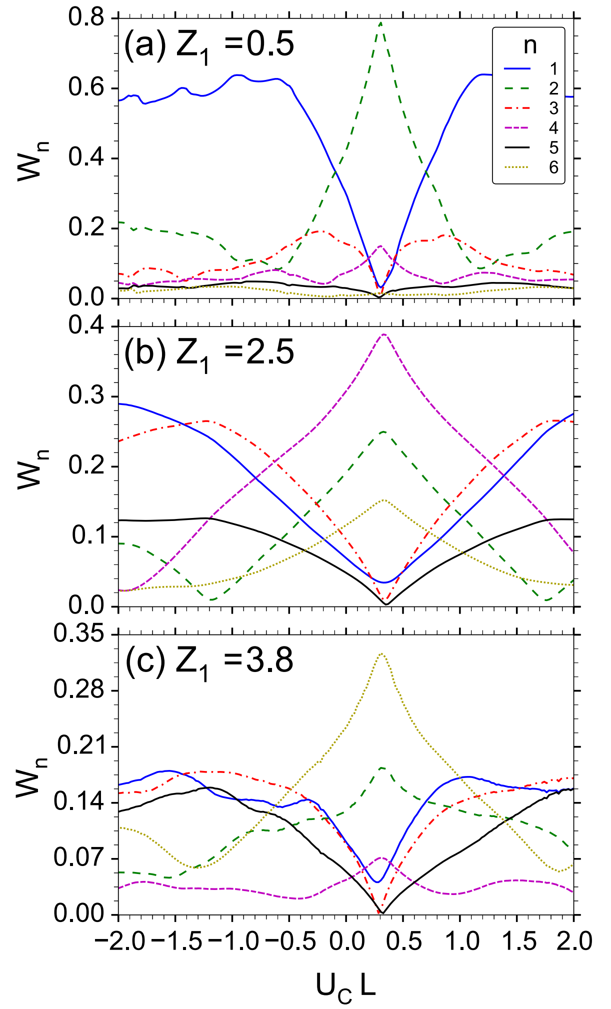

FIG. 12. High harmonic enhancement for (a) $Z_1 = 0.5$, (b) $Z_1 = 2.5$, and (c) $Z_1 = 3.8$. The parameters are $U = -10/L$, $Z_0 = 0.48\pi$, and $\Omega = 0.45/L$.

not enhanced above the first harmonic in the regime of low contact doping U, even for stronger Z_1, because the multiple resonances are not equidistant in energy space.

B. High contact doping

Next, let us study the effect of strong contact doping ($|U|$ large). See Fig. 11(a) for the angular dependence of the dc conductance in this case. A clear valley in the dc conductance is centered at the Dirac point in the central region (i.e., around $U_C = 0$), which corresponds to evanescent wave transport in the channel. The double-barrier inelastic tunneling resonances at $n\Omega = E_b$ result in a fine comb of equidistant peaks inside the valley. After integration over angles [see Fig. 11(b)], the dc conductance shows small oscillations related to the inelastic tunneling processes. Note that the weight of the resonance peak that we studied in the absence of ac drive ($Z_1 = 0$) in Fig. 3(b) has been completely redistributed across the many peaks of the comb. The peak period (Ω) is the same for all transmission channels. Therefore, analogical fine oscillations show up in ac harmonics as well; see Fig. 11(c).

In Fig. 11(c), we note that for U_C corresponding to the direct double-barrier resonance, the second harmonic is enhanced above the first harmonic, which is suppressed. By tuning parameters, we can in fact enhance a selected even n harmonic, as shown in Fig. 12, where we present the weights W_n as a function of channel doping U_C for increasing drive strength Z_1. In Figs. 12(a)–12(c), we obtain the $n = 2$, $n = 4$, and $n = 6$ harmonic, respectively. To emphasize this result, we plot the distribution between harmonics roughly on resonance ($U_C = 0.3/L$) as a function of Z_1 in Fig. 13. In the whole range of drive strengths $Z_1 > 0.25$, all odd-n harmonics are suppressed, while even-n harmonics are enhanced, one after the other.

For weak drive strength Z_1, we can show that G_1 is suppressed, while G_2 is enhanced through destructive (for G_1) and constructive (for G_2) interferences between the transmission processes responsible for the corresponding harmonic; cf. Eq. (7). To explain this behavior, we first note that Eq. (C9) tells us that sideband amplitudes t_n are proportional to $i^{|n-m|} J_{|n-m|}(Z_1)$ to lowest order in Z_1. For instance, $t_0 \propto J_0$ and $t_{\pm 1} \propto i J_1$ (symmetric). It follows that for small Z_1, the first conductance harmonic (before integration over transverse momentum) can be written as a sum of two terms involving

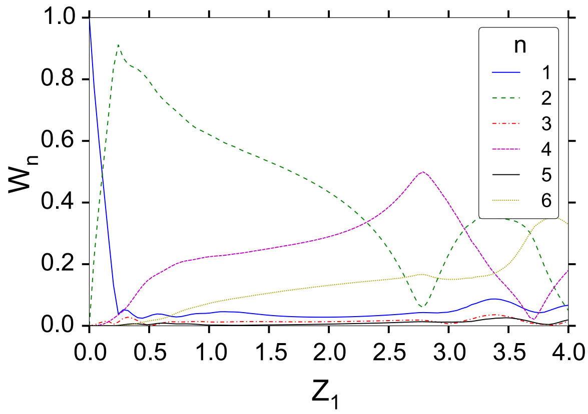

FIG. 13. High harmonic enhancement with increasing drive strength Z_1 for $U_C = 0.3/L$, corresponding to on-resonance transport. The parameters are the same as in Fig. 12.

two different transfer processes:

$$\begin{aligned} G_1(E,\varphi) &\propto t^*_{-1}(E,\varphi)t_0(E,\varphi) + t^*_0(E,\varphi)t_1(E,\varphi) \\ &= J_0 J_1[-ic_{-1}(E,\varphi) + ic_1(E,\varphi)], \end{aligned} \tag{13}$$

where $c_{\pm 1}$ are complex numbers. On resonance, $c_{-1} \approx c_1$, the two terms cancel, and G_1 is suppressed. That this symmetry appears on resonance can be seen from Fig. 5, where the peaks in $T_{\pm 1}(E_b)$ [Figs. 5(c) and 5(e)], corresponding to processes labeled 0 [Figs. 5(d) and 5(f)], have the same shape and magnitude. Off resonance, the probabilities $T_{\pm 1}(E)$ are obviously not equal, the two terms do not cancel, and G_1 is not suppressed. For the enhancement of the second harmonic, we note that for small Z_1, we have $G_2 \propto t^*_{-2}t_0 + t^*_{-1}t_1 + t^*_0 t_2$. All terms consist of real products of the coupling matrix elements M_{nm} in sideband space. On resonance, for instance, $t^*_{-2}t_0 + t^*_0 t_2 \propto J_0 J_2(c_{-2} + c_2)$ with $c_{-2} \approx c_2$, and the two terms sum up constructively because of the real coupling in sideband space. For stronger drive, the odd (even) harmonics are suppressed (enhanced) in an analogous way, where pairs of processes add up destructively (constructively).

V. SUMMARY

We have presented results for the ac conductance in a ballistic graphene field-effect transistor with a time-modulated top-gate potential, including an inhomogeneous doping profile across the device. We have studied two regimes, corresponding to (i) low doping of contacts and (ii) high doping of contacts, relative to the doping level in the channel (which is tunable by a back gate). For case (i), we find Fano resonances in direct transmission and Breit-Wigner resonances in inelastic scattering to sideband energies. The resonances are due to excitation of quasibound states in the channel, analogous to what we found in Ref. [41]. Here we have shown that these resonances survive when a moderately varying doping landscape across the device is taken into account. For case (ii), we find inelastic tunneling resonances via quasibound states in the top-gate barrier potential. For weak drive, the resonances lead to a large response in the direct current between source and drain already for weak ac drive on the top gate. We propose that the device can be utilized as a detector in the THz frequency range. In addition, for strong drive, inelastic tunneling to multiple sidebands results in resonant excitation of higher harmonics $n\Omega$ [we demonstrate dominance of $n = 6$ in Fig. 12(c)], with n an even number due to an interference effect between different tunneling processes. The harmonic n (even) can be selected either by the back gate or by tuning the drive strength. In summary, ac transport in ballistic graphene field-effect transistors is a rich subject for studying quantum mechanical resonance phenomena that can possibly also be utilized in applications such as detectors of THz radiation or to generate high harmonics.

ACKNOWLEDGMENTS

We acknowledge financial support from the Swedish Foundation for Strategic Research (SSF), the Knut and Alice Wallenberg foundation (KAW), and the Swedish Research Council. The research of O.S. was partly supported by the National Science Foundation (Grant No. DMR-1508730).

APPENDIX A: WAVE SOLUTIONS: STATIC CASE

First we derive the wave solutions to the Dirac equation without time-dependent perturbation. We assume translational invariance and conserved parallel momentum k_y, in which case the Hamiltonian has the form

$$\mathcal{H}_0 = -i\sigma_x\nabla_x + \sigma_y k_y + Z_0\delta(x) + U(x), \tag{A1}$$

where the device doping profile is described by

$$U(x) = U_L\theta(-L_1 - x) + U_R\theta(x - L_2). \tag{A2}$$

This means that in this derivation, we choose the Dirac point in the device channel, $x \in [-L_1, L_2]$, as the reference level where $E = 0$ (i.e., $U_C = 0$). The static Dirac equation

$$\mathcal{H}_0\psi(x,k_y,E) = E\psi(x,k_y,E) \tag{A3}$$

is straightforward to solve by making a plane-wave ansatz and find unknown coefficients through boundary conditions. But first it is convenient to introduce a scattering basis.

1. Scattering basis

Consider the homogeneous case, i.e., $Z_0 = 0$ and $U(x) = 0$ in Eq. (A1). The solutions, labeled by k_y and E, can be organized into a scattering basis for right- and left-moving (along the x axis) plane waves, as defined by their group velocities. This scattering basis has the form

$$\begin{aligned} \psi_{\rightarrow}(x,k_y,E) &= \frac{1}{\sqrt{2\mathrm{v}(k_y,E)}}\begin{pmatrix} 1 \\ \eta(k_y,E)\end{pmatrix} e^{i\kappa(k_y,E)x}, \\ \psi_{\leftarrow}(x,k_y,E) &= \frac{1}{\sqrt{2\mathrm{v}(k_y,E)}}\begin{pmatrix} 1 \\ \bar{\eta}(k_y,E)\end{pmatrix} e^{-i\kappa(k_y,E)x}, \end{aligned} \tag{A4}$$

where

$$\begin{aligned} \eta(k_y,E) &= \frac{\kappa(k_y,E) + ik_y}{E}, \quad \bar{\eta}(k_y,E) = \frac{-\kappa(k_y,E) + ik_y}{E}, \\ \mathrm{v}(k_y,E) &= \frac{\kappa(k_y,E)}{E}, \quad \kappa(k_y,E) = \mathrm{sgn}(E)\sqrt{E^2 - k_y^2}. \end{aligned} \tag{A5}$$

The normalization of these plane waves is such that they carry unit probability flux along the x axis, defined as

$$j_x(x,k_y,E) = \psi^\dagger(x,k_y,E)\sigma_x\psi(x,k_y,E). \tag{A6}$$

That is, we have $j_x^{\rightarrow} = 1$ and $j_x^{\leftarrow} = -1$. This scattering basis is useful in deriving the scattering matrix and computing the current within the Landauer-Büttiker formalism, as we described in detail in Ref. [41] for the case $U(x) = 0$.

$$\psi(x,k_y,E) = \begin{cases} \psi_\rightarrow(x,k_y,E-U_L) + r(k_y,E)\psi_\leftarrow(x,k_y,E-U_L), & x < -L_1 \\ a(k_y,E)\psi_\rightarrow(x,k_y,E) + b(k_y,E)\psi_\leftarrow(x,k_y,E), & -L_1 < x < 0 \\ c(k_y,E)\psi_\rightarrow(x,k_y,E) + d(k_y,E)\psi_\leftarrow(x,k_y,E), & 0 < x < L_2 \\ t(k_y,E)\psi_\rightarrow(x,k_y,E-U_R), & x > L_2. \end{cases} \tag{A8}$$

Note that the doping level in the channel region ($U_C = 0$) is different from that in the contacts (U_L and U_R). As a consequence, the waves can be evanescent in the channel region. This is included in the ansatz above by allowing $\kappa(k_y,E)$ in Eq. (A5) to be imaginary. The convention we use is that $\Psi^{\rightarrow}$ denotes a wave evanescent towards positive x, while $\Psi^{\leftarrow}$ denotes a wave evanescent in the opposite direction. This means that if $U_R \neq U_L$ and $\kappa^R = \kappa(k_y,E-U_R)$ turns imaginary, the ansatz above also holds, although in this case $t(k_y,E)$ is not a transmission amplitude. It is then eliminated in favor of the reflection coefficient $r(k_y,E)$, with $|r(k_y,E)| = 1$. This is not so important in the present discussion, but becomes important in the following section on ac transport. In the main text, we only consider the special case $U_R = U_L$ for simplicity.

The coefficients in Eq. (A8) are found through the boundary conditions, which are simple wave continuity at $x = -L_1$ and $x = L_2$, and a pseudospin rotation operation at the δ barrier (cf. Ref. [41]):

$$\psi(-L_1^-,k_y,E) = \psi(-L_1^+,k_y,E), \tag{A9}$$

$$\psi(0^-,k_y,E) = \exp[iZ_0\sigma_x]\psi(0^+,k_y,E), \tag{A10}$$

$$\psi(L_2^-,k_y,E) = \psi(L_2^+,k_y,E). \tag{A11}$$

From Eq. (A11), we can obtain $c(k_y,E)$ and $d(k_y,E)$ in terms of $t(k_y,E)$,

$$c = \sqrt{\frac{v}{v^R}}\frac{\eta^R-\bar\eta}{\eta-\bar\eta}e^{i(\kappa^R-\kappa)L_2}t, \tag{A12}$$

$$d = \sqrt{\frac{v}{v^R}}\frac{\eta-\eta^R}{\eta-\bar\eta}e^{i(\kappa^R+\kappa)L_2}t. \tag{A13}$$

Note that $v^R = v(k_y,E-U_R)$, and analogously for κ^R and η^R (also, v^L, κ^L, etc. appearing below are computed at energy $E-U_L$). The quantities in regions 1 and 2, computed at energy E, lack superscripts. Above and in the following, we suppress the explicit reference to the dependences on k_y and E unless necessary.

2. Scattering matrix derivation

Below we solve the scattering problem for quasiparticles at energy E injected from the left contact at conserved transverse momentum k_y given by

$$k_y = |E-U_L|\sin\varphi, \tag{A7}$$

where φ is the incidence angle on the scattering region, measured with respect to the x axis. There are four regions in our device: left and right contacts labeled L and R and left and right channel regions (with respect to the δ potential barrier) labeled 1 and 2. The scattering state ansatz is then

From Eq. (A10), we then obtain a and b in terms of t,

$$a = \frac{\sqrt{2v}}{\bar\eta-\eta}(\bar\eta-1)\exp[iZ_0\sigma_x]\vec{B}t, \tag{A14}$$

$$b = \frac{\sqrt{2v}}{\eta-\bar\eta}(\eta-1)\exp[iZ_0\sigma_x]\vec{B}t, \tag{A15}$$

where

$$\vec{B} = \left[\frac{\eta^R-\bar\eta}{\eta-\bar\eta}\begin{pmatrix}1\\ \eta\end{pmatrix}e^{-i\kappa L_2} + \frac{\eta-\eta^R}{\eta-\bar\eta}\begin{pmatrix}1\\ \bar\eta\end{pmatrix}e^{i\kappa L_2}\right]\frac{e^{i\kappa^R L_2}}{\sqrt{2v^R}}. \tag{A16}$$

Finally, from Eq. (A9), we obtain reflection and transmission coefficients,

$$r = \vec{C}^T\exp[iZ_0\sigma_x]\vec{B}t, \tag{A17}$$

$$t = (\vec{A}^T\exp[iZ_0\sigma_x]\vec{B})^{-1}, \tag{A18}$$

where

$$\vec{A} = \left[\frac{\bar\eta^L-\eta}{\eta-\bar\eta}\begin{pmatrix}\bar\eta\\ -1\end{pmatrix}e^{-i\kappa L_1} + \frac{\bar\eta-\bar\eta^L}{\eta-\bar\eta}\begin{pmatrix}\eta\\ -1\end{pmatrix}e^{i\kappa L_1}\right]\frac{e^{i\kappa^L L_1}}{\sqrt{2v^L}}, \tag{A19}$$

and

$$\vec{C} = \left[\frac{\eta-\eta^L}{\eta-\bar\eta}\begin{pmatrix}\bar\eta\\ -1\end{pmatrix}e^{-i\kappa L_1} + \frac{\eta^L-\bar\eta}{\eta-\bar\eta}\begin{pmatrix}\eta\\ -1\end{pmatrix}e^{i\kappa L_1}\right]\frac{e^{-i\kappa^L L_1}}{\sqrt{2v^L}}. \tag{A20}$$

The superscript T in Eqs. (A17) and (A18) denotes transposition.

3. Double-barrier tunneling

Since waves are always propagating inside the δ potential, the channel regions on either side of it form a double tunnel barrier when lead regions are highly doped such that waves are propagating there as well. It is well known that the bound state in this structure can lead to resonances in the transmission amplitude derived above. To understand it qualitatively, we write a propagation matrix that relates amplitudes a and b at the left edge of the channel to amplitudes c and d at the right edge (see Fig. 2),

$$\begin{pmatrix} a \\ b \end{pmatrix} = P_b \begin{pmatrix} c \\ d \end{pmatrix}, \tag{A21}$$

where

$$P_b = \begin{pmatrix} e^{-i\kappa L_1} & 0 \\ 0 & e^{i\kappa L_1} \end{pmatrix} \hat{D} \begin{pmatrix} e^{-i\kappa L_2} & 0 \\ 0 & e^{i\kappa L_2} \end{pmatrix}. \tag{A22}$$

The four elements of the 2×2 matrix $\hat{D}$ are obtained from the boundary condition at the δ barrier, given by Eq. (A10), as

$$D_{11} = \frac{1}{2v}(-\bar{\eta} 1) \exp[iZ_0\sigma_x] \begin{pmatrix} 1 \\ \eta \end{pmatrix}, \tag{A23}$$

$$D_{12} = \frac{1}{2v}(-\bar{\eta} 1) \exp[iZ_0\sigma_x] \begin{pmatrix} 1 \\ \bar{\eta} \end{pmatrix}, \tag{A24}$$

$$D_{21} = \frac{1}{2v}(\eta -1) \exp[iZ_0\sigma_x] \begin{pmatrix} 1 \\ \eta \end{pmatrix}, \tag{A25}$$

$$D_{22} = \frac{1}{2v}(\eta -1) \exp[iZ_0\sigma_x] \begin{pmatrix} 1 \\ \bar{\eta} \end{pmatrix}. \tag{A26}$$

For the case of evanescent waves in the channel, the wave vector becomes imaginary $\kappa = i\varkappa$ and Eq. (A22) takes the form

$$P_b = \begin{pmatrix} D_{11}e^{\varkappa L} & D_{12}e^{-\varkappa \Delta L} \\ D_{21}e^{\varkappa \Delta L} & D_{22}e^{-\varkappa L} \end{pmatrix}, \tag{A27}$$

where $L = L_1 + L_2$ and $\Delta L = L_1 - L_2$.

For a symmetric system with $\Delta L = 0$, and on resonance, i.e., when the energy E of the scattering state coincides with the δ-barrier bound state E_b, it follows from the derivation in Ref. [41] [cf. Eq. (B4)] that $D_{11} = 0$. When that happens, we see that Eq. (A21) with Eq (A27) leads to

$$a = D_{12}d, \tag{A28}$$

$$b \approx D_{21}c, \tag{A29}$$

where we also noted that $D_{22}\exp(-\kappa L) \ll D_{21}$. This shows the cross connection between decaying and exploding solutions illustrated in Fig. 2(d). When transmission is enhanced to unity, the exponential functions due to tunneling through the two barriers cancel each other. Off resonance, this clean-cut cross connection does not occur and the transmission is exponentially suppressed.

APPENDIX B: WAVE SOLUTIONS: DYNAMIC CASE

Let us now derive the Floquet scattering matrix in the presence of an oscillating δ barrier. The Hamiltonian we consider is

$$\mathcal{H} = \mathcal{H}_0 + Z_1\cos(\Omega t)\delta(x). \tag{B1}$$

The time-dependent Dirac equation

$$\mathcal{H}\psi(x,k_y,t) = i\partial_t\psi(x,k_y,t), \tag{B2}$$

including a time-periodic potential as in Eq. (B1), can be solved by making use of the Floquet ansatz:

$$\psi(x,k_y,t) = e^{-iEt}\sum_{n=-\infty}^{+\infty} e^{-in\Omega t}\psi_n(x,k_y,E). \tag{B3}$$

In analogy with the static case above, this ansatz is made in each region. Coefficients for transmitted and reflected waves are then contained in the amplitudes $\psi_n(x,k_y,E)$. The coefficients are determined through the boundary conditions. A complication in the dynamic case is the boundary condition at the oscillating δ barrier, which mixes amplitudes at different sideband energies $E_n = E + n\Omega$. Following Ref. [41], the boundary condition is best formulated by first introducing a column vector with the many sideband amplitudes $\psi_n(x,k_y,E)$,

$$\Phi(x,k_y,E) = \begin{pmatrix} \cdots \\ \psi_{-1}(x,k_y,E) \\ \psi_0(x,k_y,E) \\ \psi_1(x,k_y,E) \\ \cdots \end{pmatrix}. \tag{B4}$$

The condition to be satisfied at $x = 0$ is then

$$\Phi(0^-,k_y,E) = \check{M}\Phi(0^+,k_y,E),$$
$$\check{M} = \exp\left[iZ_0\sigma_x \otimes \check{\Gamma}_0 + i\frac{Z_1}{2}\sigma_x \otimes \check{\Gamma}_1\right], \tag{B5}$$
$$[\check{\Gamma}_0]_{n,m} = \delta_{n,m},\ \ [\check{\Gamma}_1]_{n,m} = \delta_{n,m+1} + \delta_{n,m-1}.$$

The barrier scatters an incident wave labeled by E and k_y into a linear combination of waves labeled by E_n and k_y. In the end, when calculating transport properties, we have to consider only propagating outgoing waves in the leads, $|E_n - U_L| > |k_y|$ and $|E_n - U_R| > |k_y|$. We use the following ansatz:

$$\psi_n(x,k_y,E) = \begin{cases} \delta_{n0}\psi_\rightarrow(x,k_y,E_n - U_L) + r_n\psi_\leftarrow(x,k_y,E_n - U_L), & x < -L_1 \\ a_n\psi_\rightarrow(x,k_y,E_n) + b_n\psi_\leftarrow(x,k_y,E_n), & -L_1 < x < 0 \\ c_n\psi_\rightarrow(x,k_y,E_n) + d_n\psi_\leftarrow(x,k_y,E_n), & 0 < x < L_2 \\ t_n\psi_\rightarrow(x,k_y,E_n - U_R), & x > L_2. \end{cases} \tag{B6}$$

The three boundary conditions can be written as

$$\psi_n(-L_1^-,k_y,E) = \psi_n(-L_1^+,k_y,E), \tag{B7}$$

$$\psi_n(0^-,k_y,E) = \sum_m \check{M}_{nm}\psi_m(0^+,k_y,E), \tag{B8}$$

$$\psi_n(L_2^-,k_y,E) = \psi_n(L_2^+,k_y,E). \tag{B9}$$

The steps to solve for the coefficients are analogous to the static case and we do not present them here. The resulting transmission and reflection amplitudes are computed from

$$r_n = \sum_m \vec{C}_n^T \check{M}_{nm} \vec{B}_m t_m, \tag{B10}$$

$$\sum_m \vec{A}_n^T \check{M}_{nm} \vec{B}_m t_m = \delta_{n0}, \tag{B11}$$

where

$$\vec{A}_n = \left[\frac{\bar{\eta}_n^L - \eta_n}{\eta_n - \bar{\eta}_n} \begin{pmatrix} \bar{\eta}_n \\ -1 \end{pmatrix} e^{-i\kappa_n L_1} + \frac{\bar{\eta}_n - \bar{\eta}_n^L}{\eta_n - \bar{\eta}_n} \begin{pmatrix} \eta_n \\ -1 \end{pmatrix} e^{i\kappa_n L_1} \right] \frac{e^{i\kappa_n^L L_1}}{\sqrt{2 v_n^L}}, \tag{B12}$$

$$\vec{B}_n = \left[\frac{\eta_n^R - \bar{\eta}_n}{\eta_n - \bar{\eta}_n} \begin{pmatrix} 1 \\ \eta_n \end{pmatrix} e^{-i\kappa_n L_2} + \frac{\eta_n - \eta_n^R}{\eta_n - \bar{\eta}_n} \begin{pmatrix} 1 \\ \bar{\eta}_n \end{pmatrix} e^{i\kappa_n L_2} \right] \frac{e^{i\kappa_n^R L_2}}{\sqrt{2 v_n^R}}, \tag{B13}$$

$$\vec{C}_n = \left[\frac{\eta_n - \eta_n^L}{\eta_n - \bar{\eta}_n} \begin{pmatrix} \bar{\eta}_n \\ -1 \end{pmatrix} e^{-i\kappa_n L_1} + \frac{\eta_n^L - \bar{\eta}_n}{\eta_n - \bar{\eta}_n} \begin{pmatrix} \eta_n \\ -1 \end{pmatrix} e^{i\kappa_n L_1} \right] \frac{e^{-i\kappa_n^L L_1}}{\sqrt{2 v_n^L}}. \tag{B14}$$

This system of equations for $t_n(k_y, E)$ reduces for the static case (then only t_0 is relevant) to Eq. (A18). For the case of no contact doping of the leads, i.e., $U(x) = 0$, these equations reduce to Eq. (B14) in Ref. [41].

APPENDIX C: BOUNDARY CONDITION BESSEL FUNCTION EXPANSION

In this section, we show that the boundary condition at the oscillating δ barrier in Eq. (B5) can be rewritten in terms of Bessel functions of the first kind. The matrix elements $\check{M}_{nm}$ in Eq. (B11) for transmission amplitudes, which determines the strength of sideband coupling, thereby decay with increasing $|n-m|$ as $J_{|n-m|}(Z_1)$.

The tensor $\check{M}$ in Eq. (B5) that represents the boundary condition at the δ barrier can be written as

$$\check{M} = \exp[i Z_0 \sigma_x \otimes \check{\Gamma}_0] \exp\left[i \frac{Z_1}{2} \sigma_x \otimes \check{\Gamma}_1\right]. \tag{C1}$$

We will rewrite it to highlight the sideband space distribution. We will start by expanding the ac part of it in a Taylor series,

$$\check{M}_{AC} = \exp\left[i \frac{Z_1}{2} \sigma_x \otimes \check{\Gamma}_1\right] = \sum_{l=0}^{\infty} \left(i \frac{Z_1}{2} \sigma_x\right)^l \otimes \frac{\check{\Gamma}_1^l}{l!}. \tag{C2}$$

Let us study the off-diagonal matrix $\check{\Gamma}_1$ taken to the lth power, i.e., $\check{\Gamma}_1^l$. Its matrix elements are given by binomial coefficients,

$$(\check{\Gamma}_1^l)_{nm} = \frac{l!}{\frac{l+|n-m|}{2}!\,\frac{l-|n-m|}{2}!}(l + 1 + |n-m| \mod 2), \tag{C3}$$

where $|n-m| \leqslant l$. Matrix elements for $|n-m| > l$ are zero. Let us now introduce a matrix with unity entries on its $(\pm d)$th diagonals,

$$(\check{\Gamma}_d)_{nm} = \delta_{|n-m|,d}. \tag{C4}$$

Note that $\check{\Gamma}_0$ and $\check{\Gamma}_1$ in Eq. (C1) are included in this definition. Then we can rewrite Eq. (C3) by setting $d = |n-m|$. We obtain

$$\check{\Gamma}_1^l = \sum_{d=0}^{l} \frac{l!}{\frac{l+d}{2}!\,\frac{l-d}{2}!}(l + 1 + d \mod 2)\check{\Gamma}_d. \tag{C5}$$

The Taylor series is therefore given by

$$\check{M}_{AC} = \sum_{l=0}^{\infty} \sum_{d=0}^{l} \frac{\left(i \frac{Z_1}{2} \sigma_x\right)^l \otimes \check{\Gamma}_d}{\frac{l+d}{2}!\,\frac{l-d}{2}!}(l + 1 + d \mod 2). \tag{C6}$$

By introducing a substitution $\tilde{l} = \frac{l-d}{2}$, we can rewrite it in a more convenient form,

$$\check{M}_{AC} = \sum_{\tilde{l}=0}^{\infty} \sum_{d=0}^{\infty} \frac{\left(i \frac{Z_1}{2} \sigma_x\right)^{2\tilde{l}+d} \otimes \check{\Gamma}_d}{(\tilde{l}+d)!\,\tilde{l}!}. \tag{C7}$$

Using the Bessel function of the first kind series representation,

$$J_d(Z_1) = \sum_{l=0}^{\infty} (-1)^l \frac{\left(\frac{Z_1}{2}\right)^{2l+d}}{(l+d)!\,l!}, \tag{C8}$$

we arrive at

$$\check{M}_{AC} = \sum_{d=0}^{\infty} i^d J_d(Z_1) \sigma_x^d \otimes \check{\Gamma}_d. \tag{C9}$$

Including the dc prefactor, we arrive at

$$\check{M}_{nm} = \exp[i Z_0 \sigma_x](i \sigma_x)^{|n-m|} J_{|n-m|}(Z_1). \tag{C10}$$

[1] A. C. Ferrari et al., Science and technology roadmap for graphene, related two-dimensional crystals, and hybrid systems, Nanoscale 7, 4598 (2015).

[2] F. Schwierz, Graphene transistors, Nat. Nanotechnol. 5, 487 (2010).

[3] T. Palacios, A. Hsu, and H. Wang, Applications of graphene devices in rf communications, IEEE Commun. Mag. 48, 122 (2010).

[4] M. M. Glazov and S. D. Ganichev, High frequency electric field induced nonlinear effects in graphene, Phys. Rep. 535, 101 (2014).

[5] T. Otsuji, S. A. Boubanga Tombet, A. Satou, H. Fukidome, M. Suemitsu, E. Sano, V. Popov, M. Ryzhii, and V. Ryzhii, Graphene materials and devices in terahertz science and technology, MRS Bull. **37**, 1235 (2012).
[6] F. H. L. Koppens, T. Mueller, P. Avouris, A. C. Ferrari, M. S. Vitiello, and M. Polini, Photodetectors based on graphene, other two-dimensional materials and hybrid systems, Nat. Nanotechnol. **9**, 780 (2014).
[7] R. Cheng, J. Bai, L. Liao, H. Zhou, Y. Chen, L. Liu, Y.-C. Lin, S. Jiang, Y. Huang, and X. Duan, High-frequency self-aligned graphene transistors with transferred gate stacks, Proc. Natl. Acad. Sci. USA **109**, 11588 (2012).
[8] H. Wang, D. Nezich, J. Kong, and T. Palacios, Graphene frequency multipliers, IEEE Electron Device Lett. **30**, 547 (2009).
[9] O. Habibpour, S. Cherednichenko, J. Vukusic, K. Yhland, and J. Stake, A subharmonic graphene FET mixer, IEEE Electron Device Lett. **33**, 71 (2012).
[10] L. Vicarelli, M. S. Vitiello, D. Coquillat, A. Lombardo, A. C. Ferrari, W. Knap, M. Polini, V. Pellegrini, and A. Tredicucci, Graphene field-effect transistors as room-temperature terahertz detectors, Nat. Mater. **11**, 865 (2012).
[11] M. Mittendorff, S. Winnerl, J. Kamann, J. Eroms, D. Weiss, H. Schneider, and M. Helm, Ultrafast graphene-based broadband THz detector, Appl. Phys. Lett. **103**, 021113 (2013).
[12] X. Cai, A. B. Sushkov, R. J. Suess, M. M. Jadidi, G. S. Jenkins, L. O. Nyakiti, R. L. Myers-Ward, S. Li, J. Yan, D. K. Gaskill, T. E. Murphy, H. D. Drew, and M. S. Fuhrer, Sensitive room-temperature terahertz detection via the photothermoelectric effect in graphene, Nat. Nanotechnol. **9**, 814 (2014).
[13] A. Zak, M. A. Andersson, M. Bauer, J. Matukas, A. Lisauskas, H. G. Roskos, and J. Stake, Antenna-integrated 0.6 THz FET direct detectors based on CVD graphene, Nano Lett. **14**, 5834 (2014).
[14] P. Rickhaus, P. Makk, M.-H. Liu, E. Tovari, M. Weiss, R. Maurand, K. Richter, and C. Schönenberger, Snake trajectories in ultraclean graphene p–n junctions, Nat. Commun. **6**, 1 (2015).
[15] S. Chen, Z. Han, M. M. Elahi, K. M. M. Habib, L. Wang, B. Wen, Y. Gao, T. Taniguchi, K. Watanabe, J. Hone, A. W. Ghosh, and C. R. Dean, Electron optics with ballistic graphene junctions, arXiv:1602.08182v1.
[16] Y. Zhao, J. Wyrick, F. D. Natterer, J. F. Rodriguez-Nieva, C. Lewandowski, K. Watanabe, T. Taniguchi, L. S. Levitov, N. B. Zhitenev, and J. A. Stroscio, Creating and probing electron whispering-gallery modes in graphene, Science (NY) **348**, 672 (2015).
[17] D. A. Bandurin, I. Torre, R. K. Kumar, M. Ben Shalom, A. Tomadin, A. Principi, G. H. Auton, E. Khestanova, K. S. Novoselov, I. V. Grigorieva, L. A. Ponomarenko, A. K. Geim, and M. Polini, Negative local resistance caused by viscous electron backflow in graphene, Science (NY) **351**, 1055 (2016).
[18] J. Crossno, J. K. Shi, K. Wang, X. Liu, A. Harzheim, A. Lucas, S. Sachdev, P. Kim, T. Taniguchi, K. Watanabe, T. A. Ohki, and K. C. Fong, Observation of the Dirac fluid and the breakdown of the Wiedemann-Franz law in graphene, Science (NY) **351**, 1058 (2016).
[19] F. Ghahari, H.-Y. Xie, T. Taniguchi, K. Watanabe, M. S. Foster, and P. Kim, Enhanced Thermoelectric Power in Graphene: Violation of the Mott Relation by Inelastic Scattering, Phys. Rev. Lett. **116**, 136802 (2016).
[20] E. Prada, P. San-Jose, and H. Schomerus, Quantum pumping in graphene, Phys. Rev. B **80**, 245414 (2009).
[21] L. E. F. Foa Torres, H. L. Calvo, C. G. Rocha, and G. Cuniberti, Enhancing single-parameter quantum charge pumping in carbon-based devices, Appl. Phys. Lett. **99**, 092102 (2011).
[22] P. San-Jose, E. Prada, S. Kohler, and H. Schomerus, Single-parameter pumping in graphene, Phys. Rev. B **84**, 155408 (2011).
[23] P. San-Jose, E. Prada, H. Schomerus, and S. Kohler, Laser-induced quantum pumping in graphene, Appl. Phys. Lett. **101**, 153506 (2012).
[24] S. A. Mikhailov and K. Ziegler, New Electromagnetic Mode in Graphene, Phys. Rev. Lett. **99**, 016803 (2007).
[25] S. A. Mikhailov and K. Ziegler, Nonlinear electromagnetic response of graphene: frequency multiplication and the self-consistent-field effects, J. Phys.: Condens. Matter **20**, 384204 (2008).
[26] S. V. Syzranov, M. V. Fistul, and K. B. Efetov, Effect of radiation on transport in graphene, Phys. Rev. B **78**, 045407 (2008).
[27] K. L. Ishikawa, Nonlinear optical response of graphene in time domain, Phys. Rev. B **82**, 201402(R) (2010).
[28] H. L. Calvo, P. M. Perez-Piskunow, S. Roche, and L. E. F. Foa Torres, Laser-induced effects on the electronic features of graphene nanoribbons, Appl. Phys. Lett. **101**, 253506 (2012).
[29] I. Al-Naib, J. E. Sipe, and M. M. Dignam, High harmonic generation in undoped graphene: Interplay of inter- and intraband dynamics, Phys. Rev. B **90**, 245423 (2014).
[30] C. Sinha and R. Biswas, Transmission of electron through monolayer graphene laser barrier, Appl. Phys. Lett. **100**, 183107 (2012).
[31] S. A. Jafari, Nonlinear optical response in gapped graphene, J. Phys.: Condens. Matter **24**, 205802 (2012).
[32] H. K. Avetissian, A. K. Avetissian, G. F. Mkrtchian, and K. V. Sedrakian, Multiphoton resonant excitation of Fermi-Dirac sea in graphene at the interaction with strong laser fields, J. Nanophoton. **6**, 061702 (2012).
[33] H. K. Avetissian, G. F. Mkrtchian, K. G. Batrakov, S. A. Maksimenko, and A. Hoffmann, Multiphoton resonant excitations and high-harmonic generation in bilayer graphene, Phys. Rev. B **88**, 165411 (2013).
[34] B. Trauzettel, Y. M. Blanter, and A. F. Morpurgo, Photon-assisted electron transport in graphene: Scattering theory analysis, Phys. Rev. B **75**, 035305 (2007).
[35] M. A. Zeb, K. Sabeeh, and M. Tahir, Chiral tunneling through a time-periodic potential in monolayer graphene, Phys. Rev. B **78**, 165420 (2008).
[36] C. G. Rocha, Luis E. F. Foa Torres, and G. Cuniberti, ac transport in graphene-based Fabry-Pérot devices, Phys. Rev. B **81**, 115435 (2010).
[37] S. E. Savel'ev, W. Häusler, and P. Hänggi, Current Resonances in Graphene with Time-Dependent Potential Barriers, Phys. Rev. Lett. **109**, 226602 (2012).
[38] W.-T. Lu, S.-J. Wang, W. Li, Y.-L. Wang, C.-Z. Ye, and H. Jiang, Fano-type resonance through a time-periodic potential in graphene, J. Appl. Phys. **111**, 103717 (2012).

[39] L. Z. Szabó, M. G. Benedict, A. Czirják, and P. Földi, Relativistic electron transport through an oscillating barrier: Wave-packet generation and Fano-type resonances, Phys. Rev. B **88**, 075438 (2013).
[40] R. Zhu, J.-H. Dai, and Y. Guo, Fano resonance in the nonadiabatically pumped shot noise of a time-dependent quantum well in a two-dimensional electron gas and graphene, J. Appl. Phys. **117**, 164306 (2015).
[41] Y. Korniyenko, O. Shevtsov, and T. Löfwander, Resonant second-harmonic generation in a ballistic graphene transistor with an ac-driven gate, Phys. Rev. B **93**, 035435 (2016).
[42] P. F. Bagwell and R. K. Lake, Resonances in transmission through an oscillating barrier, Phys. Rev. B **46**, 15329 (1992).
[43] M. H. Pedersen and M. Büttiker, Scattering theory of photon-assisted electron transport, Phys. Rev. B **58**, 12993 (1998).
[44] G. Platero and R. Aguado, Photon-assisted transport in semiconductor nanostructures, Phys. Rep. **395**, 1 (2004).
[45] S. Kohler, J. Lehmann, and P. Hänggi, Driven quantum transport on the nanoscale, Phys. Rep. **406**, 379 (2005).
[46] B. Huard, N. Stander, J. A. Sulpizio, and D. Goldhaber-Gordon, Evidence of the role of contacts on the observed electron-hole asymmetry in graphene, Phys. Rev. B **78**, 121402 (2008).
[47] We note that for a system translationally invariant in the transverse direction, one has to compute conductance per unit length. In our previous work (cf. Eqs. (D10)–(E2) in Ref. [41]), we missed the $1/2\pi$ prefactor associated with k_y integration in the current and conductance formulas, which we include here [see Eq. (7)]. The main results of Ref. [41] are not affected, although the scales in Figs. 3(b) and 4 should include this prefactor.
[48] J. Tworzydło, B. Trauzettel, M. Titov, A. Rycerz, and C. W. J. Beenakker, Sub-Poissonian Shot Noise in Graphene, Phys. Rev. Lett. **96**, 246802 (2006).
[49] B. Ricco and M. Y. Azbel, Physics of resonant tunneling. The one-dimensional double-barrier case, Phys. Rev. B **29**, 1970 (1984).
[50] H. Yamamoto, Resonant tunneling condition and transmission coefficient in a symmetrical one-dimensional rectangular double-barrier system, Appl. Phys. A **42**, 245 (1987).
[51] R. Danneau, F. Wu, M. F. Craciun, S. Russo, M. Y. Tomi, J. Salmilehto, A. F. Morpurgo, and P. J. Hakonen, Shot Noise in Ballistic Graphene, Phys. Rev. Lett. **100**, 196802 (2008).
[52] G. Giovannetti, P. A. Khomyakov, G. Brocks, V. M. Karpan, J. Van Den Brink, and P. J. Kelly, Doping Graphene with Metal Contacts, Phys. Rev. Lett. **101**, 026803 (2008).
[53] A. Laitinen, G. S. Paraoanu, M. Oksanen, M. F. Craciun, S. Russo, E. Sonin, and P. Hakonen, Contact doping, Klein tunneling, and asymmetry of shot noise in suspended graphene, Phys. Rev. B **93**, 115413 (2016).